Ion doping simultaneously increased the carrier density and modified the conduction type of Sb2Se3 thin films towards quasi-homojunction solar cell

G. Liang, X. Chen, D. Ren, X. Jiang, R. Tang, Z. Zheng, Z. Su, P. Fan, Xianghua Zhang, Y. Zhang, et al.

G. Liang, X. Chen, D. Ren, X. Jiang, R. Tang, et al.. Ion doping simultaneously increased the carrier density and modified the conduction type of Sb2Se3 thin films towards quasi-homojunction solar cell. Journal of Materiomics, 2021, 7 (6), pp.1324-1334. 10.1016/j.jmat.2021.02.009 . hal-03420560

HAL Id: hal-03420560
https://hal.science/hal-03420560v1

Submitted on 2 Jun 2022

Journal of Materiomics 7 (2021) 1324–1334

Contents lists available at ScienceDirect

Journal of Materiomics

journal homepage: www.journals.elsevier.com/journal-of-materiomics/

Ion doping simultaneously increased the carrier density and modified the conduction type of Sb_2Se_3 thin films towards quasi-homojunction solar cell

Guangxing Liang [a], Xingye Chen [a], Donglou Ren [b], Xiangxing Jiang [a], Rong Tang [a], Zhuanghao Zheng [a], Zhenghua Su [a], Ping Fan [a], Xianghua Zhang [b], Yi Zhang [c], Shuo Chen [a, *]

[a] Shenzhen Key Laboratory of Advanced Thin Films and Applications, Key Laboratory of Optoelectronic Devices and Systems of Ministry of Education and Guangdong Province, College of Physics and Optoelectronic Engineering, Shenzhen University, Shenzhen, 518060, China
[b] Univ Rennes, CNRS, ISCR (Institut des Sciences Chimiques de Rennes) UMR 6226, F-35000, Rennes, France
[c] Tianjin Key Laboratory of Photoelectronic Thin Film Devices and Technology, Renewable Energy Conversion and Storage Center, Nankai University, Tianjin, 300350, China

ARTICLE INFO

Article history:
Received 25 November 2020
Received in revised form
13 February 2021
Accepted 17 February 2021
Available online 23 February 2021

Keywords:
Sb_2Se_3
Thin film
Ion doping
Carrier density
Quasi-homojunction solar cell

ABSTRACT

Antimony selenide (Sb_2Se_3) has drawn tremendous research attentions in recent years as an environment-friendly and cost-efficient photovoltaic material. However, the intrinsic low carrier density and electrical conductivity limited its scope of applications. In this work, an effective ion doping strategy was implemented to improve the electrical and photoelectrical performances of Sb_2Se_3 thin films. The Sn-doped and I-doped Sb_2Se_3 thin films with controllable chemical composition can be prepared by magnetron sputtering combined with post-selenization treatment based on homemade plasma sintered targets. As a result, the Sn-doped Sb_2Se_3 thin film exhibited a great increase in carrier density by several orders of magnitude, by contrast, a less increase with one order of magnitude was achieved for the I-doped Sb_2Se_3 thin film. Additionally, such cation or anion doping could simultaneously modify the conduction type of Sb_2Se_3, enabling the first fabrication of a substrate structured Sb_2Se_3-based quasi-homojunction thin film solar cell with configuration of Mo/Sb_2Se_3-Sn/Sb_2Se_3-I/ITO/Ag. The obtained power conversion efficiency exceeding 2% undoubtedly demonstrated its attractive photovoltaic application potential and further investigation necessity.

1. Introduction

In recent decades, solar cells have drawn tremendous research interest due to their sustainable, renewable and environment-friendly power source of solar energy[1,2]. As a new generation of photovoltaic devices, thin film solar cells show attractive application potential thanks to their advantages of low material consumption, high power generation and the scalable flexibility[3–5]. Among them, the representative copper indium gallium selenide (CIGS) and cadmium telluride (CdTe) solar cells have achieved impressive power conversion efficiencies (PCEs) of 23.35% and 22.1% at the laboratory scale, possessing a non-ignorable market share[6]. Nevertheless, the involved scarce elements of In, Ga, and Te, and/or toxic element of Cd could inevitably hinder their further development to a multi-terawatt level. Thus, alternative cost-efficient and environment-friendly semiconductor materials are widely explored to broaden its scope of applications in thin film photovoltaic scenarios.

Antimony selenide (Sb_2Se_3) is an inorganic V-VI binary compound with only one stable orthorhombic phase, its elemental constitutes of Sb and Se also possess advantages of low toxicity, low cost and earth abundance. It has emerged as promising photovoltaic candidate because of its attractive optoelectronic properties, such as an appropriate band gap (1.1–1.3 eV, approaching the ideal Shockey-Queisser value), large absorption coefficient ($>10^5$ cm^{-1}), decent carrier mobility (~10 cm^{2}V^{-1}s^{-1}) and long carrier lifetime (~60 ns)[7–9]. During the last decade, Sb_2Se_3 solar cells have been

---

[*] Corresponding author.
E-mail address: chensh@szu.edu.cn (S. Chen).
Peer review under responsibility of The Chinese Ceramic Society.

https://doi.org/10.1016/j.jmat.2021.02.009

extensively investigated, presenting a significant improvement of PCEs from less than 2%[10] to a record 7.6%[11] for planar heterojunction configuration and a champion 9.2%[8] for core-shell Sb_2Se_3 nanorod array structure. Despite such great endeavors, it is still far behind its Shockley-Queisser (S-Q) limit efficiency of above 30% [12]. Analysis of the key device parameters, the short-circuit current density (J_{SC}) and fill factor (FF) of the state-of-the-art Sb_2Se_3 solar cells have reached 70% of their S-Q limits, but the open-circuit voltage (V_{OC}) with a ratio less than 50% seems a core bottleneck for further breakthrough of device efficiency[12]. Such large Voc deficit (Eg/q-Voc) can be attributed to the severe recombination caused by the surface/interface trap states and/or defects/impurities in bulk [12,13]. For the critical absorber layer, the deep-level defects (i.e., V_{Se}, Sb_{Se}, and Se_{Sb}) could be fairly diminished by optimizing the fabrication process. However, the experimental-dependent free carrier density of undoped Sb_2Se_3 is only 10^{13} cm^{-3}, far lower than the optimal doping density for absorber layer (~10^{16} cm^{-3}), limiting the quasi-Fermi level splitting and thus primarily limit the Voc [14,15]. Up to now, some attempts have been made to increase the carrier density of Sb_2Se_3, but the results are still unsatisfactory [14,16].

Doping with extrinsic ions is an efficient way to increase the carrier density of the absorber layer. For instance, Chen et al. demonstrated that sodium ion doping could simultaneously regulate the hole concentration of the CIGS absorber layer as well as the device Voc[17]. Metzger et al. reported that polycrystalline CdTe films with group V arsenic doping could realize a significant increase of major-carrier density with 3 orders of magnitude, resulting a device efficiency of 20.8%[18]. In contrast, the research on Sb_2Se_3 thin films with effectively increased carrier density has been rarely reported, which is closely related to its intrinsic 1D chainlike structure of $(Sb_4Se_6)_n$ ribbons with wide spacing (~0.35 nm) to easily locate the dopants between ribbons. Our previous work, including the enhanced electrical conductivity of $(Sn_xSb_{1-x})_2Se_3$ nanorods prepared by hot-injection method and Sn-doped Sb_2Se_3 bulk crystals prepared by melt-quenching method [19,20], the efficient Sb_2Se_3-based quasi-homojunction thin film solar cell with superstrate configuration of ITO/$Sb_2Se_{3.3}$/$Sb_2(Se_{0.9}I_{0.1})_3$/Au[21], suggesting the possibility of successful ion doping in Sb_2Se_3 and certainly needs further exploration.

In this work, tin (Sn) and iodine (I) were respectively chosen as cation dopant and anion dopant to simultaneously increase the carrier density and modify the conduction type of Sb_2Se_3 thin films. A facile method of ball milling followed with spark plasma sintering (SPS) was firstly used to prepare the pre-designed Sb_2Se_3-based sputtering targets, then a high energy process of magnetron sputtering (almost two times energetic compared to general thermal evaporation process) was implemented to obtain Sb_2Se_3-based thin films with ideal substitutional doping. An increased carrier density and improved photoelectric performance have been successfully fulfilled through such ion doping. Finally, a substrate structured Sb_2Se_3-based quasi-homojunction thin film solar cell with configuration of Mo/Sb_2Se_3-Sn/Sb_2Se_3-I/ITO/Ag was fabricated for the first time and achieved an interesting PCE of 2.17%. This work offers a new research direction for solving intrinsic low carrier density of Sb_2Se_3 thin films and exploring applications as advantageous quasi-homojunction solar cells.

2. Experimental section

2.1. Preparation of Sb_2Se_3-based targets

An effective and scalable method of ball milling combined with SPS process was used to prepare the Sb_2Se_3-based targets. High-purity Sb_2Se_3 powder (99.99%, Advanced Material Professional Manufacture, 100 meshes), Sn powder (99.99%, Aladdin, 100 meshes) and I particles (99.99%, Aladdin) were used as raw materials. A schematic illustration of the preparation process is shown in Fig. 1a. Taking Sn (1 wt%)-doped Sb_2Se_3 target as an example, 35 g Sb_2Se_3 powder and 0.35 g Sn powder were put into a stainless cell with steel balls and kept milling for 5 h in a vertical planetary ball mill. The SPS process of the as-milled mixed powder was carried out by using an apparatus Labox-325 SPS, performing under a fixed pressure of 30 kN, a temperature of 420 °C with heating rate of 20 °C/min and a dwell of 5 min. Finally, the sputtering target with diameter of 60 mm and thickness of 2 mm could be obtained by finely surface polishing of the SPS processed bulk sample.

2.2. Preparation of Sb_2Se_3-based thin films

Sb_2Se_3-based thin films were prepared using radio frequency (RF) magnetron sputtering based on the aforementioned home-made targets, an additional post-selenization heat treatment was applied to contribute efficient crystallization, as depicted in Fig. 1c and d. In detail, Mo-coated soda lime glass with sequential cleaning treatment of detergent, ethanol solution and deionized water, was chosen as substrate. The deposition chamber was evacuated to a residual pressure of less than 8.0×10^{-4} Pa before running the deposition procedures. High-purity argon gas was introduced at a rate of 40 sccm, the sputtering power was fixed to 25 W also with a low deposition pressure of 1.0 Pa to ensure essential compactness. Afterwards, a post-selenization heat treatment was carried out in a double-chamber vacuum tubular furnace with separately placing the as-deposited Sb_2Se_3-based thin film and high-purity Se particles (99.999%, particle size: 1–6 mm, Aladdin). Temperature of the Se side was kept at 400 °C to provide sufficient Se partial pressure, selenization of the thin films was last for 20 min at temperatures of 350 °C, 400 °C and 450 °C, respectively.

2.3. Preparation of Sb_2Se_3 quasi-homojunction thin film solar cells

Herein, for the first time, a substrate structured Sb_2Se_3 quasi-homojunction thin film solar cell with configuration of Mo/Sb_2Se_3-Sn/Sb_2Se_3-I/ITO/Ag was fabricated. The Sb_2Se_3-Sn and Sb_2Se_3-I layer was successively sputtered with respective thickness of 800 nm and 100 nm, then undergoing a synchronous post-selenization heat treatment. Indium tin oxide (ITO) window layer was sputtered under a power of 120 W, a pressure of 0.4 Pa, a flow rate of 30 sccm for argon and 8 sccm for oxygen gas. Finally, the conductive Ag patterns was thermally evaporated on the surface and it was scribed into small squares with identical active device area of 0.15 cm^2 (Fig. 1e).

2.4. Characterizations

The crystal structure of Sb_2Se_3-based thin films were characterized by X-ray diffraction (XRD, Ultima-IV) with CuKα radiation under 40 kV and 40 mA. The quality and composition of the thin films were also analyzed by X-ray photoelectron spectroscopy (XPS, Thermo ESCALAB 250Xi). Morphologies of the thin films were obtained using a Zeiss SUPRA 55 thermal field emission scanning electron microscope (SEM). A Shimadzu UV-3600 UV/Vis/NIR spectrophotometer equipped with monochromator was used for the optical reflectance and transmittance investigation by using pure soda-lime glass (SLG) as the substrate. Electrical properties of the Sb_2Se_3-based thin films were measured using a Hall-effect measurement system with Van der Pauw configuration (HL5500PC, 200 Nanometrics). The photo-electro-chemical (PEC) properties of the thin films were characterized by cyclic voltammograms and chronoamperometry measurements with K050

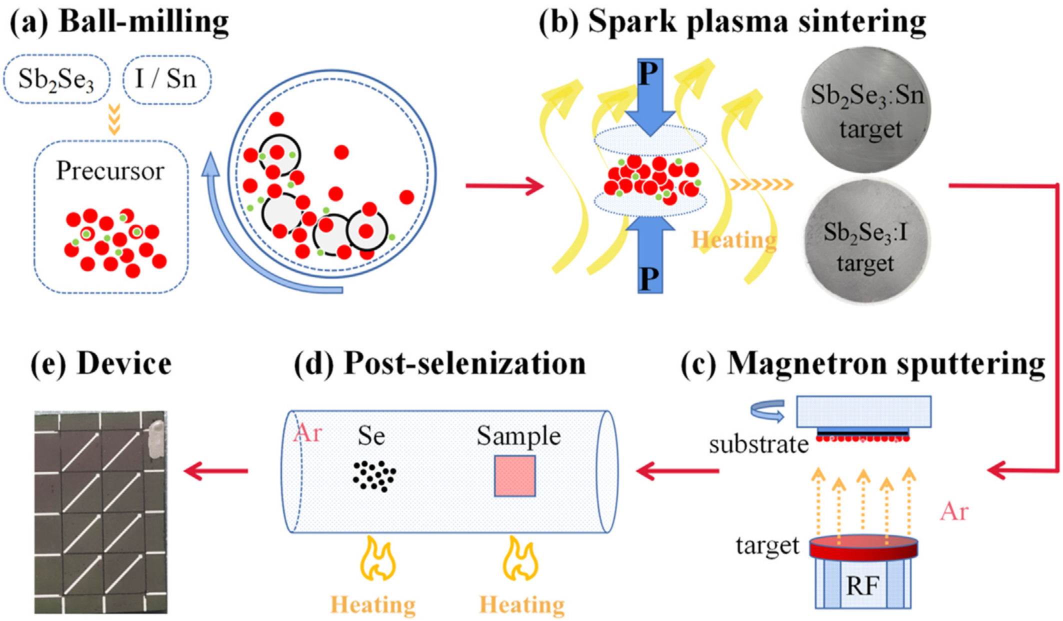

Fig. 1. Schematic illustration of the preparation process of the Sb_2Se_3 quasi-homojunction thin film solar cell. (a) Sn-doped and I-doped Sb_2Se_3 fine powder obtained by ball milling, (b) Sb_2Se_3-based target obtained by SPS process, (c) Sb_2Se_3-based thin film deposition by RF magnetron sputtering, (d) Post-selenization heat treatment, (e) Representative photograph of the device, surface morphology of the device after Ag electrode painted.

photochemical electrolytic cell under AM 1.5G light illumination. Current density-voltage (J-V) curves of the Sb_2Se_3 quasi-homojunction thin film solar cells were obtained using a multimeter (Keithley, 2400 Series) under AM 1.5G light illumination with intensity calibrated to 100 mW/cm^2 through a Si reference cell. External quantum efficiency (EQE) measurements were also implemented using a Zolix SCS101 system.

3. Results and discussion

The Sb_2Se_3-based thin films were prepared using magnetron sputtering combined with post-selenization heat treatment based on homemade targets. For convenience, the pure Sb_2Se_3, Sn-doped Sb_2Se_3 with 1 wt% doping concentration and I-doped Sb_2Se_3 with 5 wt% doping concentration are labeled as C, C-Sn-1% (or C-Sn) and C-I-5% (or C-I), respectively. Fig. 2a shows the XRD patterns of the C-Sn target and the corresponding C-Sn thin films at different post-selenization temperatures. It can be seen that all the diffraction peaks of the C-Sn target match well with the JCPDS standard card (No. 15–0861) of the orthorhombic phase of Sb_2Se_3 without detectable impurity. The absence of second phase can be attributed to a slight difference in atomic radius between Sb (0.160 nm) and Sn (0.158 nm) that satisfies the criterion for substitution solubility proposed by Hume-Rothery[20]. Moreover, the obtained target has a rather ideal relative density as high as 98% measured by using Archimedes drainage method. Combined with a smooth and compact surface morphology, as depicted in Fig. 1b, the SPS produced target meets the requirement for magnetron sputtering. An obvious state transition from amorphous as-deposited C-Sn thin film to crystalline post-selenized thin films can be observed, indicating an effective thermally induced crystallization under Se environment. The sharp and matched diffraction peaks also indicate its highly crystalline nature, and an accurate composition transfer from target to thin films. Moreover, an emerging preferential growth orientation of (hk1) has been attached to the crystalline C-Sn thin film, which is really beneficial for reducing the recombination loss at grain boundaries and promoting the photo-generated carriers transport through absorber layer, according to recent theoretical and experimental studies[22,23]. Analogously, XRD patterns of the as-prepared C-I target and C-I thin films are shown in Fig. 2b, presenting a similar Sb_2Se_3 matrix determined evolution. However, an additional diffraction peak ($2\theta = 29.4°$) belonging to (112) crystalline plane of orthorhombic SbSeI (JCPDS Card No. 38–0691) can also be observed for the C-I target and C-I thin film post-selenized at 450 °C. Such phenomenon is probably because a high doping concentration and high temperature treatment that induced excess I and Se to form second phase under enough thermodynamic energy. Importantly, the result of C-I thin film post-selenized at 400 °C also indicates an effective substitutional doping. To further confirm the successful ion doping, XPS characterizations have been implemented to the aforementioned C-Sn-1% and C-I-5% thin films after post-selenization at 400 °C, accompanied by two suchlike C-Sn-10% and C-I-10% thin films with significantly higher doping concentration. As shown in Fig. 2c, compared to pure Sb_2Se_3 (C), two observable peaks located at 494.8 and 486.5 eV indicated the existence of Sn^{4+} ions, which is in accordance with our pre-designed cation doping. Similarly, the spin-orbit-coupled doublet of the I 3d core levels of C-I-5% and C-I-10% thin films are split into $3d_{5/2}$ (~630.4 eV) and $3d_{3/2}$ (~618.9 eV) with increased intensity and a fixed separation binding energy value of 11.5 eV (Fig. 2d), such typical I^- characters further confirmed the successful anion doping in Sb_2Se_3[24].

Fig. 3 presents the SEM images of the as-deposited and post-selenized Sb_2Se_3-based thin films at temperatures of 350 °C, 400 °C and 450 °C, respectively. As shown in Fig. 3a and e, both the as-deposited C-Sn and C-I thin films show amorphous nature, in agreement with XRD results. The observed fine particles were formed due to limited kinetic energy and weak surface diffusion during the sputtering process. After post-selenization at 350 °C–400 °C, an obvious thermally induced crystallization and densification of the C-Sn thin films can be observed, accompanied by a synchronous increase of average grain size from approximately 350 nm–1200 nm (Fig. 3b and c). However, further increasing the temperature to 450 °C, the formation of distinct micro-voids was

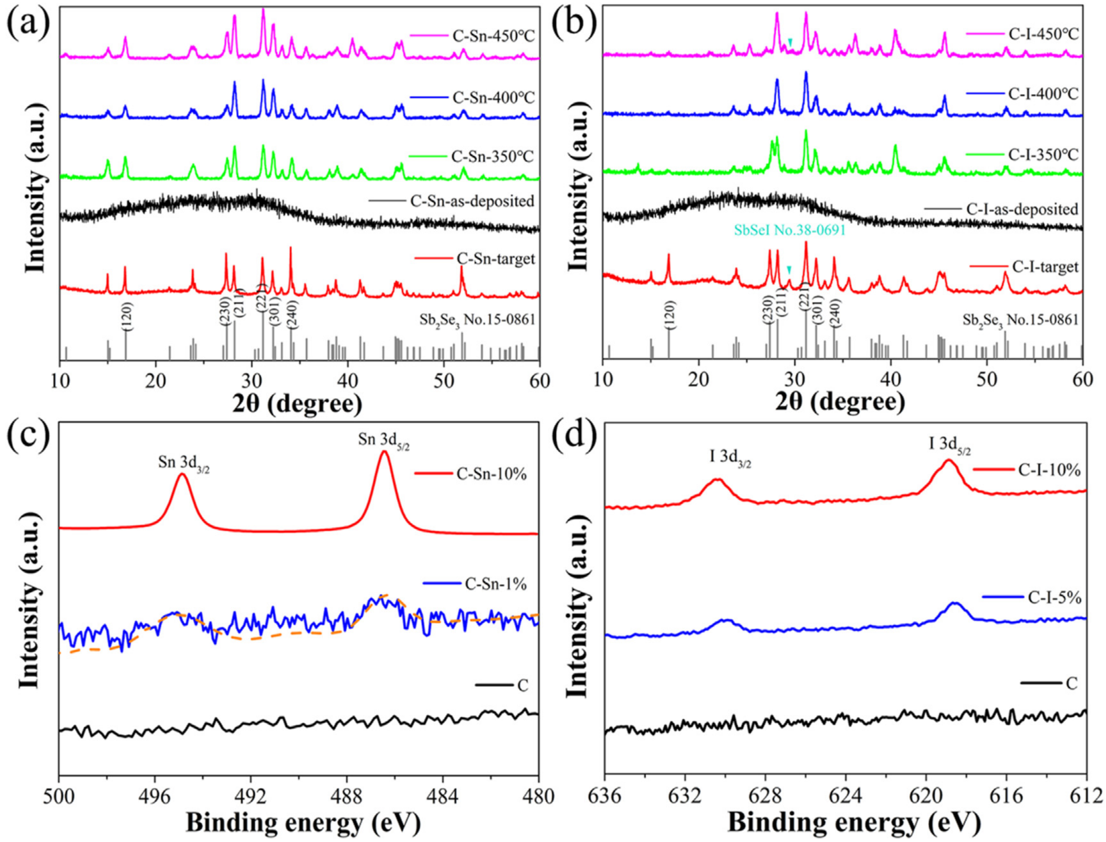

Fig. 2. XRD patterns of the C-Sn (a) and C–I (b) homemade targets and the corresponding thin films post-selenized at different temperatures. XPS spectra of Sn-3d (c) and I-3d (d) for the Sb_2Se_3-based thin films.

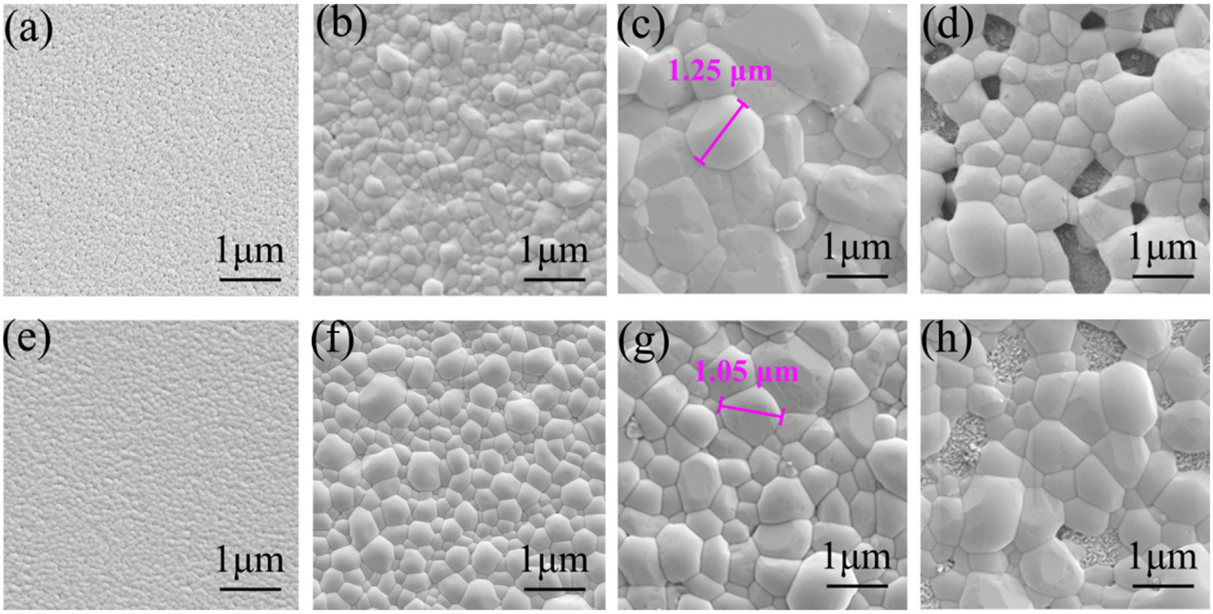

Fig. 3. Top-view SEM images of the C-Sn (a–d) and C–I (e–h) thin films under deposition and post-selenization at temperatures of 350 °C, 400 °C and 450 °C, respectively.

reasonable to occur due to Se evaporated from the pristine thin film under its naturally high vapor pressure, as depicted in Fig. 3d. Similarly, a dense and uniform crystalline C-I thin film with an average grain size of approximately 1000 nm can be obtained at a post-selenization temperature of 400 °C (Fig. 3g). A slightly different surface morphology evolution and grain size decrease for C-I thin film as compared to C-Sn thin film indicate the doping ions have participated and affected this crystallization and growth process. Overall, it is crucial to control the post-selenization temperature to simultaneously obtain high-quality C-Sn and C-I thin film, enable the achievement of efficient quasi-homojunction solar cells.

The optical properties of the Sb_2Se_3-based thin films were characterized by UV/Vis/NIR spectrophotometer. Fig. 4 shows the reflection and transmission spectra of C-Sn and C-I thin films using glass as substrate and the wavelength of incident light ranges from 300 nm to 1600 nm. As shown in Fig. 4a and d, obvious reflection curves shift between the as-deposited amorphous thin film and the post-selenized crystalline thin films can be observed, which is closely related to its structure-dependent atomic arrangement and density-dependent refractive index[25]. Moreover, the reflectance of the amorphous C-Sn and C-I thin film lies at approximately 40% in the short wavelength absorption region, then a slight value variation for the selenized thin films are caused by interior crystallinity and surface roughness. According to the transmission spectra (Fig. 4b and e), a synchronous red-shift of the cut-off edge from 705 nm for the amorphous C-Sn thin film to about 980 nm for the crystalline C-Sn thin film and 670 nm for the amorphous C-I thin film to about 930 nm for crystalline C-I thin film, both clearly imply a decrease of band gap after post-selenization heat treatment. The specific band gap value can be calculated according to the following formulas:

$$\alpha = \frac{1}{d}\ln\left(\frac{1-R(\lambda)}{T(\lambda)}\right) \tag{1}$$

$$\alpha h\nu = C\left(h\nu - E_g\right)^n \tag{2}$$

where α is the absorption coefficient, d is the thickness of thin film, R is the reflectance, T is the transmittance, h is the Planck's constant, v is the photon frequency, C is a constant, n is an index defined by 2.0 for indirect and 0.5 for direct band gap semiconductor, respectively [26,27]. As shown in Fig. 4c, after linear extrapolating of the (αhv)2 versus hv curve, the as-deposited amorphous C-Sn thin film has a direct band gap Eg of 1.68 eV, then the value decrease to 1.12 eV and 1.10 eV for the crystalline C-Sn thin films underwent 350 °C and 400 °C post-selenization. An abnormal band gap of 1.02 eV belonging to the C-Sn thin film selenized at 450 °C can be attributed to the composition deviation and compactness damage at high temperature, as corroborated by SEM result. Fig. 4f shows a similar temperature-dependent band gap evolution for the C-I thin films, except for a slight value expansion possibly caused by doping induced Burstein-Moss shift [28]. Notably, these doped thin films possess optimum band gap as efficient light absorber layer in photovoltaic scenarios.

Electrical properties of the absorber material are important parameters to be considered when designing and optimizing the device configuration. The study on Sb_2Se_3 thin film is really lacking because of its intrinsic low electrical conductivity ($10^{-6}\ \Omega^{-1}\ m^{-1}$), which is a considerable challenge for obtaining electrical properties directly from Hall effect measurement. Herein, the electrical conductivity, carrier density, mobility and the conduction type of Sb_2Se_3-based thin films were systematically characterized through an effect temperature-dependent Hall effect process. The insulative soda-lime glass (SLG) was used as substrate for depositing Sb_2Se_3-based thin films and four symmetric gold plots as electrodes with Ohmic contact were subsequently deposited on the surface via sputtering. Fig. 5a shows the temperature-dependent electrical conductivity (σ) of pure Sb_2Se_3 (C) thin film, Sn-doped Sb_2Se_3 (C-Sn-1% and C-Sn-10%) thin films in the temperature (T) range of 100 °C–200 °C. An obvious positive correlation between the electrical conductivity and temperature confirmed typical semiconductor characteristics. The significant increase of lnσ value also indicates an increase of conductivity after Sn doping. Moreover, the conductivity σ exhibits nearly single activation energy in the measuring temperature range, which can be described by the following Arrhenius equation:

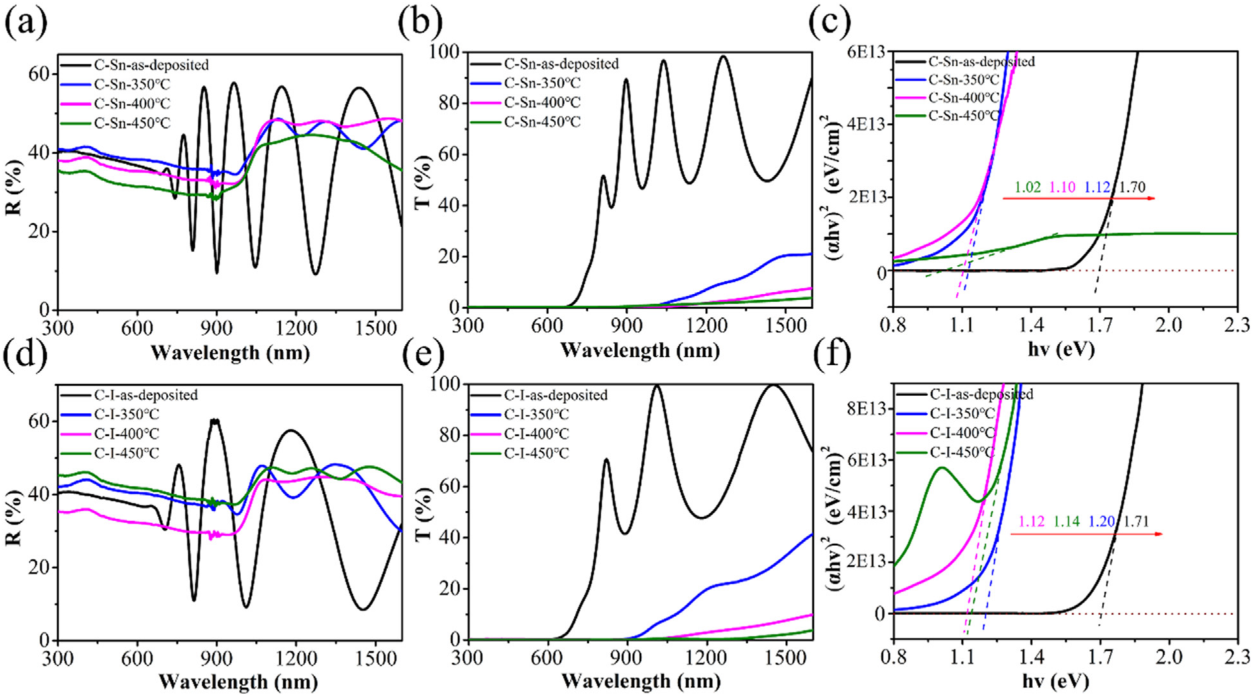

Fig. 4. Optical characterization of the C-Sn (a–c) and C–I (d–f) thin films as a function of wavelength and with different post-selenization temperatures. (a, d) Reflection spectra, (b, e) Transmission spectra, (c, f) Plot of $(\alpha hv)^2$ versus hv, used to obtain direct band gap.

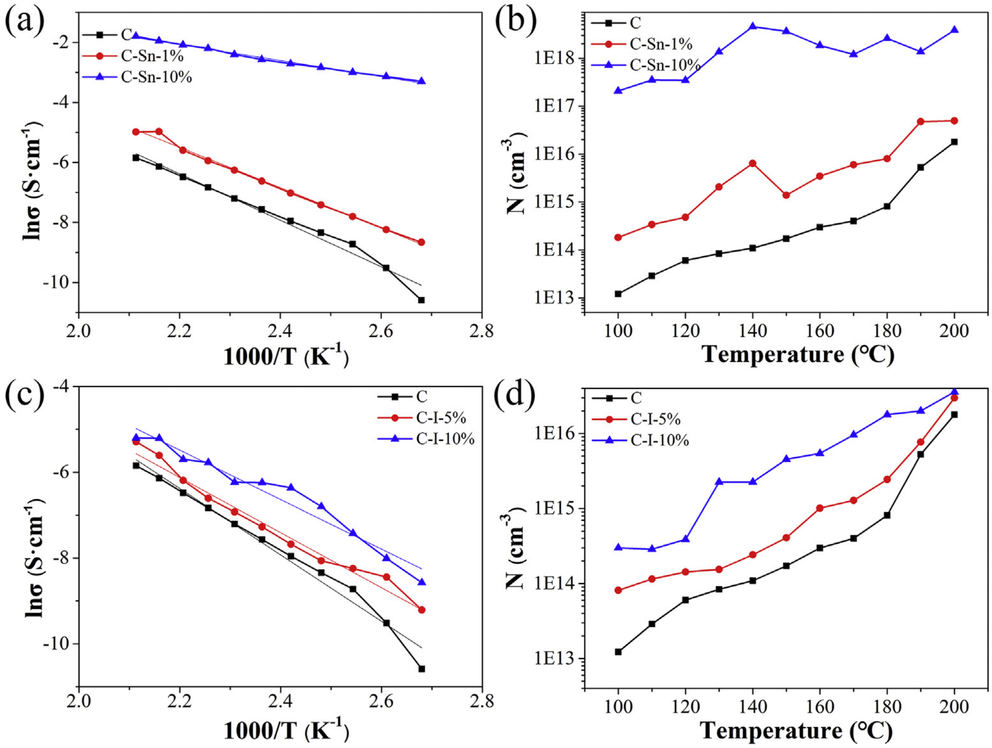

Fig. 5. Temperature-dependent electrical conductivity (σ) and carrier density (n) of C-Sn thin films (a, b) and C–I thin films (c, d) with different doping concentration and covering a temperature (T) range of 100–200 °C during Hall effect measurements.

$$\sigma = \sigma_0 \exp\left(-\frac{\Delta E}{kT}\right) \tag{3}$$

where σ_0 is the pre-exponential factor, ΔE is the thermal activation energy and k is the Boltzmann constant[29]. Thus ΔE and σ_0 can be calculated from the slope and the intercept on the y-axis of the $\ln\sigma_0$ versus 1/T curve, respectively. Then the temperature-dependent carrier density (n) of the C thin film and C-Sn thin films are depicted in Fig. 5b, presenting an obvious increase of carrier density with increasing doping concentration and testing temperature. In parallel, temperature-dependent σ and n of pure Sb_2Se_3 (C) thin film, I-doped Sb_2Se_3 (C-I-5% and C-I-10%) thin films are shown in Fig. 5c and d, respectively. The same variation tendency confirmed an effect ion doping, a smaller growth rate is closely related to its efficient doping concentration and ionization rate associated to the dopants, i.e., I ion possesses high vapor pressure. Finally, all the electrical properties of Sb_2Se_3-based thin films determined by Hall effect measurements at 100 °C are summarized in Table 1. Obviously, pure Sb_2Se_3 thin film exhibits extremely low electrical conductivity of 2.52×10^{-5} s cm^{-1}, then the value increase to 1.72×10^{-4} s cm^{-1} and 3.66×10^{-2} s cm^{-1} for C-Sn thin films with 1% and 10% doping concentration, 1.67×10^{-4} s cm^{-1} and 3.32×10^{-4} s cm^{-1} for C-I thin films with 1% and 10% doping concentration, respectively, accompanied by a synchronous increase of carrier density. According to the typical expression:

$$\sigma = ne\mu \tag{4}$$

where n is the carrier density, μ is the carrier mobility and e is the unit charge[30]. Considering that μ values decrease after doping, the dominant factor that accounts for the increase of σ is the increase of n caused by extrinsic ions induced effective substitutional doping. The calculated ΔE values show a decrease trend after doping, which is consistent with its theoretically prediction since it varies inversely with the charge carrier density. The obtained σ_0 could modify by the increase of localized state density created by doping induced composition and configuration disorder. Importantly, Table 1 also shows the C-Sn thin films and C-I thin films present P-type and N-type conduction behaviors, respectively. It demonstrates that such ion doping can simultaneously increase the carrier density and modify the conduction type of Sb_2Se_3, enabling the design of novel quasi-homojunction thin film solar cells.

Table 1
A summary of electrical properties of the Sb_2Se_3-based thin films at 100 °C.

Sample	σ	n	μ	σ_0	△E	Conduction
	($s \cdot cm^{-1}$)	(cm^{-3})	(V·s)	($s \cdot cm^{-1}$)	(eV)	type
C	2.52×10^{-5}	1.21×10^{13}	12.9	4.22×10^{4}	0.67	P
C-Sn-1%	1.72×10^{-4}	1.82×10^{14}	5.9	1.10×10^{4}	0.58	P
C-Sn-10%	3.66×10^{-2}	2.07×10^{17}	1.11	4.43×10^{1}	0.23	P
C-I-5%	1.67×10^{-4}	1.03×10^{14}	10.1	2.98×10^{3}	0.55	N
C-I-10%	3.32×10^{-4}	2.99×10^{14}	6.9	1.35×10^{3}	0.50	N

The photoconductive characteristics of the Sb_2Se_3-based thin films were investigated using the classical 3-electrode photo-electro-chemical (PEC) measurements. Fig. 6a shows a representative schematic configuration, where Ag/AgCl electrode in 3.5 M KCl was used as the reference electrode, Pt-wire as the counter electrode and the Sb_2Se_3-based thin film deposited on ITO substrate was used as working electrode. These electrodes were simultaneously immersed into the electrolyte (0.1 $mol \cdot L^{-1}$ Na_2SO_4 solution) and undergoing AM 1.5G light illumination. The chopped light can be obtained by a mechanical chopper at a frequency of 5 Hz. Fig. 6b-d shows the current density versus voltage curves using 400 °C post-selenized C, C-Sn and C-I thin films as the working electrode, respectively. As shown in Fig. 6b, the Sb_2Se_3 crystalline thin film can produce a photocurrent density

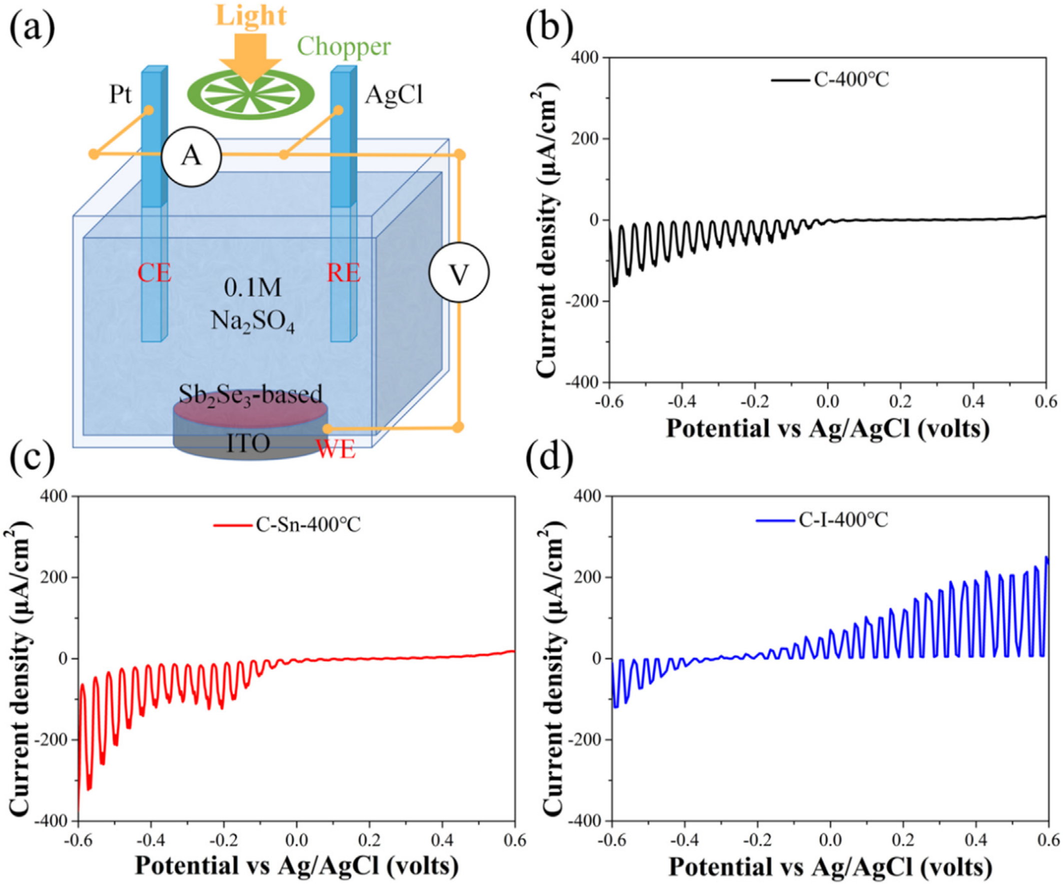

Fig. 6. (a) Schematic diagram of the 3-electrode photo-electro-chemical (PEC) measurement. (b–d) Current density-voltage characteristics using C thin film, C-Sn thin film and C–I thin film as working electrode, respectively.

of −170 μA/cm^2 at −0.6 V, suggesting its photoelectric effect. For C-Sn thin film (Fig. 6c), by comparison, the dark current density increased from −24 μA/cm^2 to −64 μA/cm^2 at a negative bias voltage of −0.6 V, confirming the enhancement of electrical conductivity after Sn doping, then the photocurrent density also dramatically increased from −170 μA/cm^2 to −345 μA/cm^2, presenting much superior photoelectric properties. Interestingly, an obvious photo-response under positive bias condition can be observed for C-I thin film (Fig. 6d), implying a reverse of conduction type. Since the minority carriers in the space charge region will participate in charge transport in the presence of a depletion layer, the enhanced current density under positive bias during PEC measurement indicates its N-type conductive character[31]. Thus, the PEC-determined conduction type for Sb_2Se_3-based thin films are consistent with the information given by Hall effect measurements. Explanatorily, the dopant Sn with one fewer valence electron than Sb can constitute hole doping under appropriate substitution, however, the dopant I can replace the lattice position of Se and play a strong electron donor role.

The stability and response speed of the Sb_2Se_3-based thin film working electrode were also characterized by chronoamperometry measurements with PEC equipment. Fig. 7a-c shows the time-resolved PEC response using C, C-Sn and C-I crystalline thin film as the working electrode, respectively. As shown in Fig. 7a, when the light was on, the current density rapidly increased from −55 μA/cm^2 (dark condition) to −160 μA/cm^2 (with 100 mW cm^{-2} light illumination). Once the light was off, the current density rapidly returned to its initial value, such “on/off” circle can remain the same after more than 10 times, suggesting the excellent reversibility and stability of this Sb_2Se_3 thin film PEC electrode. For C-Sn thin film working electrode, the same phenomenon can be observed except for a larger dark current and photocurrent (Fig. 7b), which is closely related to ion doping induced increase of carrier density. An obvious time-resolved PEC response under positive bias (+0.6 V) is consistent with its N-type conductive nature. To extract the specific response time, one of the response periods is magnified, as shown in Fig. 7d-f. In the time domain, the response time (τ_{on}) and the recovery time (τ_{off}) of the C thin film working electrode are both 0.09 s, then these two evaluated values decrease to 0.09 s and 0.07 s for C-Sn thin film, both 0.07 s for C-I thin film, respectively. Such interesting evolution can be explained by doping induced the introduction of interfacial states and surface dangling bonds to decrease the electron-hole recombination. Furthermore, it is worth noting that the fast response speed is comparable to some outstanding results of the previously reported high performance photoelectric devices [32,33].

Up to now, state-of-the-art Sb_2Se_3 solar cells generally used CdS, ZnO or TiO_2 as buffer layer to construct planar heterojunction configuration[9,11,34]. Only a few preliminary attempts have been applied to Sb_2Se_3-based quasi-homojunction thin film solar cells with superstrate structure, reported by our group[21,35]. Herein, taking the features of quasi-homojunction device structure with theoretical advantages, i.e., eliminating solution processed buffer layer, highly efficient light absorption and well-matched interfacial lattice, a novel Sb_2Se_3-based quasi-homojunction thin film solar cell with substrate structure of Mo/Sb_2Se_3-Sn/Sb_2Se_3-I/ITO/Ag was prepared for the first time. Fig. 8a shows a schematic illustration as

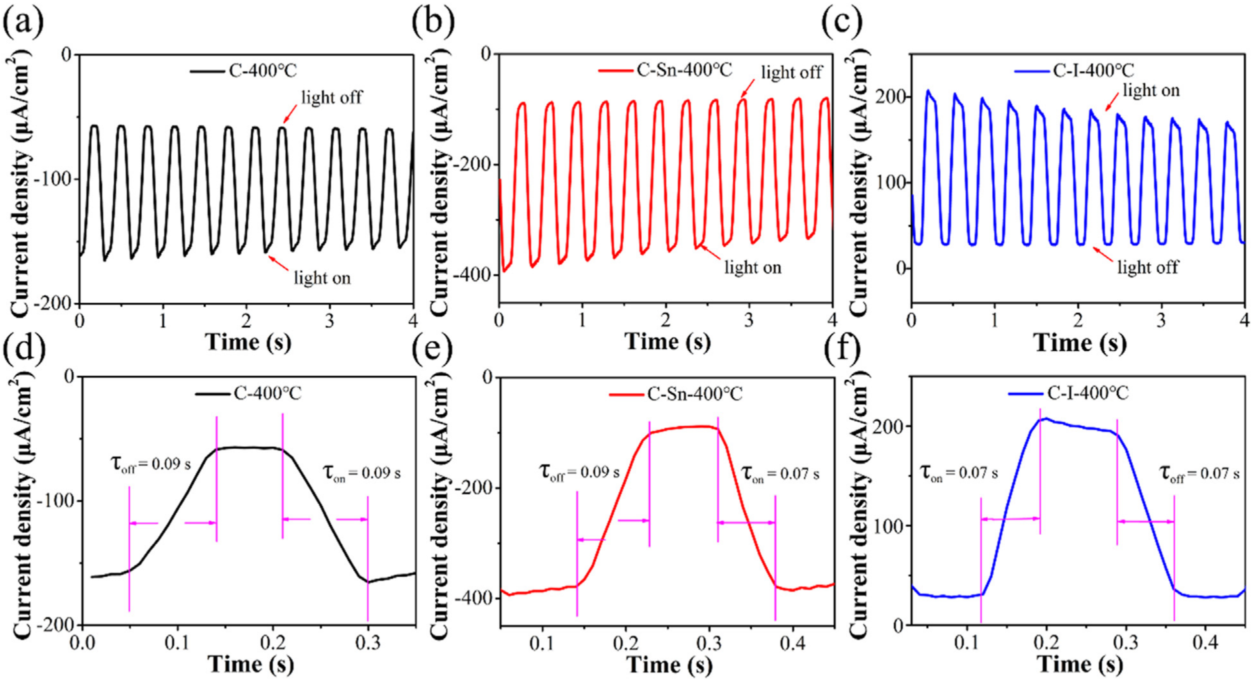

Fig. 7. Time-resolved PEC photoresponse using C (a), C-Sn (b) and C–I (c) thin film as the working electrode, respectively. (d–f) The corresponding magnified one response cycle, used to obtain the response time and recovery time.

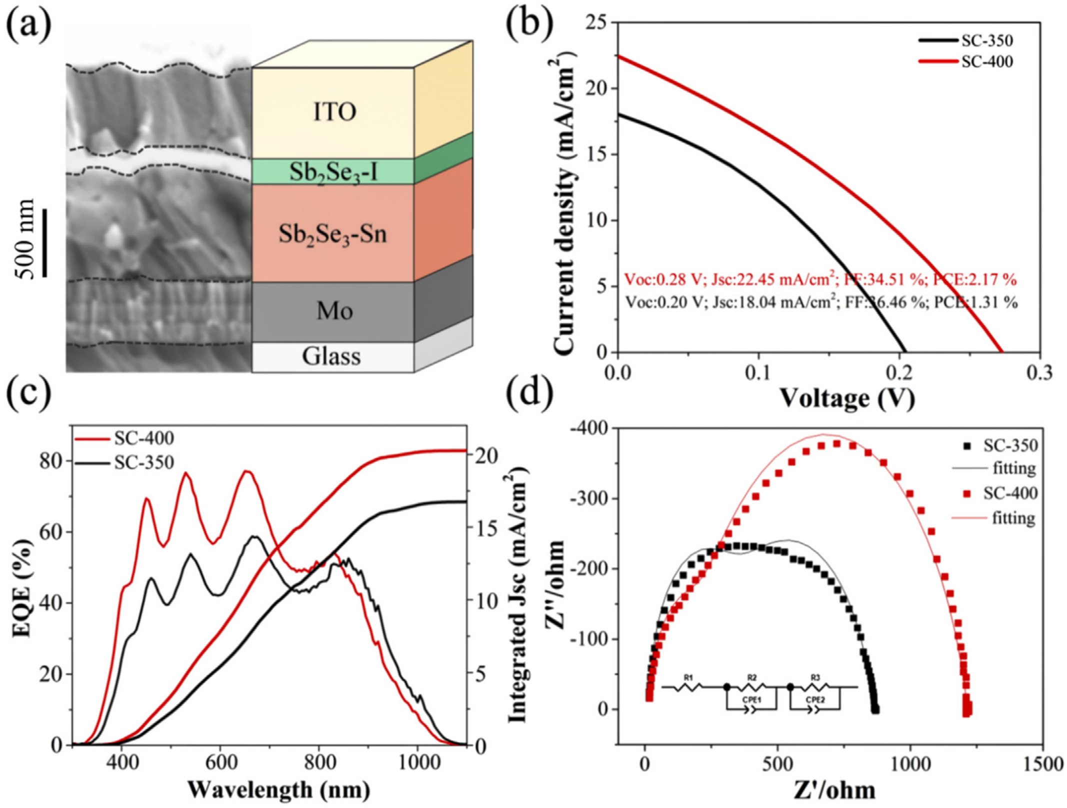

Fig. 8. (a) Schematic illustration and cross-sectional SEM image of the substrate structured Sb_2Se_3-based quasi-homojunction thin film solar cell, (b) J-V curves, (c) EQE and integrated J_{SC}, and (d) Nyquist plots of the representative SC-350 and SC-400 devices.

well as a representative cross-sectional SEM image of this device. It displays obvious layered structure with approximate thickness of 800 nm, 120 nm and 550 nm for Sb_2Se_3-Sn, Sb_2Se_3-I and ITO layer, respectively. Moreover, the well-adherent and pinhole-free interface is really beneficial for reducing charge carrier recombination and current leakage. Two representative quasi-homojunction solar

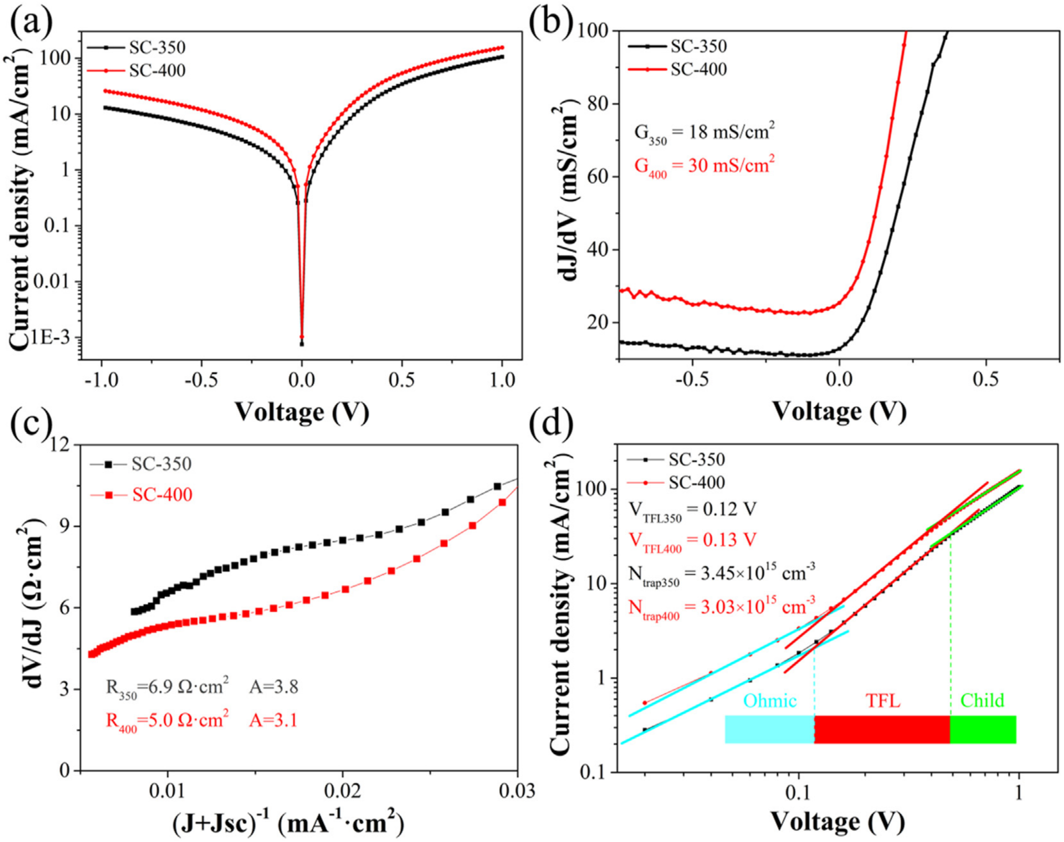

Fig. 9. Electrical behaviors of the representative SC-350 and SC-400 devices: (a) Dark J-V curves, (b) shunt conductance G, (c) series resistance R and ideality factor A, (d) logarithmic J-V curves with Ohmic, TFL and Child regions.

cells based on Sb_2Se_3-Sn/Sb_2Se_3-I duplex thin films post-selenized at 350 °C and 400 °C are denoted as SC-350 and SC-400, respectively. According to the current density-voltage (J-V) curves, as shown in Fig. 8b, the SC-350 device gives a J_{SC} of 18.04 mA/cm^2, V_{OC} of 0.20 V, FF of 36.46% and a PCE of 1.31%. In contrast, the SC-400 device shows an improvement with J_{SC} of 22.45 mA/cm^2, V_{OC} of 0.28 V, FF of 34.51%, and an interesting PCE of 2.17%. Such important improvement can be attributed to the 400 °C selenized Sb_2Se_3-based absorbing thin film with better crystallinity, larger crystal grains and much benign growth orientation, which is consistent with the XRD and SEM results. This preliminary exploration already demonstrates an effective design of this substrate structured quasi-homojunction thin film solar cell, further absorber engineering (i.e., doping concentration, defects control, growth control) and interfacial engineering (i.e., band alignment, back contact) should be implemented in future research. Fig. 8c shows the external quantum efficiency (EQE) spectra of these two devices, a broad response region (up to ~1100 nm) is in accordance with the narrow band gap of Sb_2Se_3-based thin films. The integrated J_{SC} calculated from EQE data are 16.76 mA/cm^2 and 20.28 mA/cm^2, respectively, which are also comparable to the J-V measurement results. Meanwhile, electrochemical impedance spectroscopy (EIS) was used to characterize the carrier transport properties of the device. Fig. 8d shows Nyquist plots of the SC-350 and SC-400 devices, which were measured in the frequency range from 1 to 10^6 Hz under darkness with a 30 mV AC amplitude. Each plot possesses two quasi-semicircles covering the whole frequency region, obtained by fitting the EIS data. An equivalent circuit diagram (inset in Fig. 8d) consists of a sheet resistance (R1), contact resistance (R2) and recombination resistance (R3). In detail, R1 extracting mainly from the substrate shows a similar value of approximately 19 Ω for both devices. The high frequency feature can be ascribed to R2, associated with the Sb_2Se_3-Sn/Sb_2Se_3-I quasi-homojunction interfaces, the fitted values are 274.5 Ω and 143 Ω for those two devices, implying the SC-400 device has a better interfacial contact. Finally, a higher R3 value for SC-400 device also reveals an essentially suppressed charge recombination, leading to a higher J_{SC} and V_{OC}.

The junction-dependent electrical behaviors of the SC-350 and SC-400 devices were further analyzed by dark J-V measurements. As shown in Fig. 9a, obvious rectifying characteristics for both devices can be observed. According to the general single exponential diode equation:

$$J = J_0 \exp\left[\frac{q}{AkT}(V - RJ)\right] + GV - J_L \quad (5)$$

where J_0 is reverse saturation current density, q is the elementary charge, A is diode ideality factor, R is series resistance, G is shunt conductance and J_L is light current density[36]. Fig. 9b presents the plots of dJ/dV against V, where the G values can be obtained by reading from the flat regions under reverse bias, thus the SC-400 device possesses a higher G value of 30 mS•cm^{-2} than 18 mS•cm^{-2} belonging to the SC-350 device. The series resistance R and the diode ideality factor A were obtained by plotting dV/dJ against $(J + J_{SC})^{-1}$ to extract the intercept and slope, respectively (Fig. 9c). After linear fitting, the R can be specified to 6.9 Ω cm^2 and 5.0 Ω cm^2 for SC-350 and SC-400 device, respectively. Meanwhile, the obtained A values were 3.8 and 3.1, implying the existence of nonuniformity of trap levels in the depletion region at the Sb_2Se_3-Sn/Sb_2Se_3-I quasi-homojunction interface that induced interface recombination and space-charge region (SCR) recombination, and a less nonradiative recombination loss for SC-400 device[12,37]. The defect states were further investigated according to a standard space charge limited current model[38]. As shown in Fig. 9d, the logarithmic J-V curve can be divided into three regions, including the Ohmic region (at low voltages), the trap-filled limit (TFL) region (at intermediate voltages) and the Child region (at high voltages). The obtained onset voltages of TFL region (V_{TFL}) were 0.12 and 0.13 eV for SC-350 and SC-400 device, respectively. Then the trap state density N_{trap} can be estimated with the following equation:

$$N_{trap} = \frac{2\varepsilon\varepsilon_0 V_{TFL}}{qL^2} \tag{6}$$

where L is the Sb_2Se_3-based thin film thickness, q is the elementary charge, ϵ is the relative dielectric constant and ϵ_0 is the vacuum permittivity[39]. By comparison, the N_{trap} value shows a decrease from 3.45×10^{15} cm^{-3} for SC-350 to 3.03×10^{15} cm^{-3} for SC-400 device, suggesting that the 400 °C post-selenized thin film possesses much superior quality with less trap sites and/or defect centers. Importantly, the SC-400 device with larger shunt conductance, better ideality factor, smaller series resistance and less trap state density confirmed an efficient Sb_2Se_3-Sn/Sb_2Se_3-I quasi-homojunction and an improved junction quality under appropriate post-selenization heat treatment, further demonstrating its great photovoltaic application potential.

4. Conclusions

In summary, an effective Sb_2Se_3 associated ion doping strategy with tin (Sn) and iodine (I) respectively chosen as cation dopant and anion dopant has been successfully developed. A facile method of ball milling combined with SPS process was firstly used to prepare the composition designed Sn-doped and I-doped Sb_2Se_3 targets, then high-quality Sb_2Se_3-based thin films can be obtained by RF magnetron sputtering followed with an additional post-selenization heat treatment. A systematic investigation of crystalline phase, surface morphologies, optical properties, electrical properties and photoelectric properties evolution confirmed an ideal ion doping in Sb_2Se_3 thin film. Importantly, the Sn-doped Sb_2Se_3 thin film exhibited a great increase in carrier density by several orders of magnitude, a less increase with one order of magnitude was also achieved for the I-doped Sb_2Se_3 thin film. Such ion doping could simultaneously modify the conduction type, leading to P-type and N-type characters for Sb_2Se_3-Sn and Sb_2Se_3-I thin films, respectively. Accordingly, a substrate structured Sb_2Se_3-based quasi-homojunction thin film solar cell with configuration of Mo/Sb_2Se_3-Sn/Sb_2Se_3-I/ITO/Ag was fabricated for the first time and the efficiency reached already an interesting 2.17%. The combined features of absorbing thin films with controllable preparation and properties, solar cells with advantageous substrate and quasi-homojunction configuration, which undoubtedly demonstrated its great application potential in thin film photovoltaic scenarios.

Declaration of competing interest

The authors declare that they have no known competing financial interests or personal relationships that could have appeared to influence the work reported in this paper.

Acknowledgements

This work was supported by Natural Science Foundation of Guangdong Province (2020A1515010805) China, National Natural Science Foundation of China (No. 62074102), Key Project of Department of Education of Guangdong Province (No. 2018KZDXM059) China, Science and Technology plan project of Shenzhen (JCYJ20190808153409238) China.

References

[1] Tang RF, Wang XM, Lian WT, Huang JL, Wei Q, Huang ML, Yin YW, Jiang CH, Yang SF, Xing GC, Chen SY, Zhu CF, Hao XJ, Green MA, Chen T. Hydrothermal deposition of antimony selenosulfide thin films enables solar cells with 10% efficiency. Nat. Energy 2020;5:587–95.

[2] Kondrotas R, Chen C, Tang J. Sb_2S_3 solar cells. Joule 2018;2:857–78.

[3] Liang GX, Luo YD, Chen S, Tang R, Zheng ZH, Li XJ, Liu XS, Liu YK, Li YF, Chen XY, Su ZH, Zhang XH, Ma HL, Fan P. Sputtered and selenized Sb_2Se_3 thin-film solar cells with open-circuit voltage exceeding 500 mV. Nano Energy 2020;73:104806.

[4] Polman A, Knight M, Garnett EC, Ehrler B, Sinke WC. Photovoltaic materials: present efficiencies and future challenges. Science 2016;352:aad4424.

[5] Yan C, Huang JL, Sun KW, Johnston S, Zhang YF, Sun H, Pu AB, He MR, Liu FY, Eder K, Yang LM, Cairney JM, Ekins-Daukes NJ, Hameiri Z, Stride JA, Chen SY, Green MA, Hao XJ. Cu_2ZnSnS_4 solar cells with over 10% power conversion efficiency enabled by heterojunction heat treatment. Nat. Energy 2018;3:764–72.

[6] Green MA, Dunlop ED, Hohl-Ebinger J, Yoshita M, Kopidakis N, Hao XJ. Solar cell efficiency tables (version 56). Prog. Photovolt. 2020;28:629–38.

[7] Shen K, Zhang Y, Wang X, Ou C, Guo F, Zhu H, Liu C, Gao Y, Schropp REI, Li Z, Liu X, Mai Y. Efficient and stable planar n–i–p Sb_2Se_3 solar cells enabled by oriented 1D trigonal selenium structures. Adv Sci 2020:2001013.

[8] Li Z, Liang X, Li G, Liu H, Zhang H, Guo J, Chen J, Shen K, San X, Yu W, Schropp REI, Mai Y. 9.2%-efficient core-shell structured antimony selenide nanorod array solar cells. Nat Commun 2019;10:125.

[9] Wang L, Li DB, Li K, Chen C, Deng HX, Gao L, Zhao Y, Jiang F, Li L, Huang F, He Y, Song H, Niu G, Tang J. Stable 6%-efficient Sb_2Se_3 solar cells with a ZnO buffer layer. Nat. Energy 2017;2:17046.

[10] Luo M, Leng M, Liu X, Chen J, Chen C, Qin S, Tang J. Thermal evaporation and characterization of superstrate CdS/Sb_2Se_3 solar cells. Appl Phys Lett 2014;104:173904.

[11] Wen X, Chen C, Lu S, Li K, Kondrotas R, Zhao Y, Chen W, Gao L, Wang C, Zhang J, Niu G, Tang J. Vapor transport deposition of antimony selenide thin film solar cells with 7.6% efficiency. Nat Commun 2018;9:2179.

[12] Chen C, Tang J. Open-circuit voltage loss of antimony chalcogenide solar cells: status, origin and possible solution. ACS Energy Lett 2020;5:2294–304.

[13] Yang Z, Wang X, Chen Y, Zheng Z, Chen Z, Xu W, Liu W, Yang Y, Zhao J, Chen T, Zhu H. Ultrafast self-trapping of photoexcited carriers sets the upper limit on antimony trisulfide photovoltaic devices. Nat Commun 2019;10:4540.

[14] Guo C, Liang X, Liu T, Liu Y, Yang L, Lai W, Schropp REI, Song D, Mai Y, Li Z. 1D/3D alloying induced phase transition in light absorbers for highly efficient Sb_2Se_3 solar cells. Sol. RRL 2020;4:2000054.

[15] Lei H, Chen J, Tan Z, Fang G. Review of recent progress in antimony chalcogenide-based solar cells: materials and devices. Sol. RRL 2019:1900026.

[16] Chen C, Wang L, Gao L, Nam D, Li D, Li K, Zhao Y, Ge C, Cheong H, Liu H, Song H, Tang J. 6.5% certified efficiency Sb_2Se_3 solar cells using PbS colloidal quantum dot film as hole-transporting layer. ACS Energy Lett 2017;2:2125–32.

[17] Yuan ZK, Chen S, Xie Y, Park JS, Xiang H, Gong XG, Wei SH. Na-diffusion enhanced p-type conductivity in Cu(in, Ga)Se_2: a new mechanism for efficient doping in semiconductors. Adv. Energy Mater. 2016;6:1601191.

[18] Metzger WK, Grover S, Lu D, Colegrove E, Moseley J, Perkins CL, Li X, Mallick R, Zhang W, Malik R, Kephart J, Jiang CS, Kuciauskas D, Albin DS, Al-Jassim MM, Xiong G, Gloeckler M. Exceeding 20% efficiency with in situ group V doping in polycrystalline CdTe solar cells. Nat. Energy 2019;4:837–45.

[19] Chen S, Shehzad K, Qiao XS, Luo X, Liu XM, Zhang YT, Zhang XH, Xu Y, Fan XP. A high performance broadband photodetector based on $(Sn_xSb_{1-x})_2Se_3$ nanorods with enhanced electrical conductivity. J Mater Chem C 2018;6:11078–85.

[20] Chen S, Qiao X, Zheng Z, Cathelinaud M, Ma H, Fan X, Zhang X. Enhanced electrical conductivity and photoconductive properties of Sn-doped Sb_2Se_3 crystals. J Mater Chem C 2018;6:6465–70.

[21] Chen S, Zheng Z, Cathelinaud M, Ma H, Qiao X, Su Z, Fan P, Liang G, Fan X, Zhang X. Magnetron sputtered Sb_2Se_3-based thin films towards high performance quasi-homojunction thin film solar cells. Sol Energy Mater Sol Cells 2019;203:110154.

[22] Zhou Y, Wang L, Chen S, Qin SX, Liu, Chen J, Xue DJ, Luo M, Cao Y, Cheng Y, Sargent EH, Tang J. Thin-film Sb_2Se_3 photovoltaics with oriented one-dimensional ribbons and benign grain boundaries. Nat Photon 2015;9:409–15.

[23] Chen C, Bobela DC, Yang Y, Lu S, Zeng K, Ge C, Yang B, Gao L, Zhao Y, Beard MC, Tang J. Characterization of basic physical properties of Sb_2Se_3 and its relevance for photovoltaics. Front Optoelectron 2017;10:18–30.

[24] Chen S, Li F, Chen YX, Luo JT, Liang GX, Zhang XH, Zheng ZH, Fan P. Enhanced thermoelectric properties of Sb_2Te_3/CH_3NH_3I hybrid thin films by post-annealing. Inorg. Chem. Front. 2020;7:198–203.

[25] Luo J, Xiong W, Liang G, Liu Y, Yang H, Zheng Z, Zhang X, Fan P, Chen S. Fabrication of Sb_2S_3 thin films by magnetron sputtering and post-sulfurization/selenization for substrate structured solar cells. J Alloys Compd

2020;826:154235.

[26] Kobayashi T, Kumazawa T, Kao ZJL, Nakada T. Cu(In,Ga)Se_2 thin film solar cells with a combined ALD-Zn(O,S) buffer and MOCVD-ZnO:B window layers. Sol Energy Mater Sol Cells 2013;119:129–33.

[27] Liang G, Chen X, Tang R, Liu Y, Li Y, Luo P, Su Z, Zhang X, Fan P, Chen S. Spark plasma sintering of Sb_2Se_3 sputtering target towards highly efficient thin film solar cells. Sol Energy Mater Sol Cells 2020;211:110530.

[28] Gibbs ZM, LaLonde A, Snyder GJ. Optical band gap and the Burstein–Moss effect in iodine doped PbTe using diffuse reflectance infrared Fourier transform spectroscopy. New J Phys 2013;15:075020.

[29] Bronnikov S, Podshivalov A, Kostromin S, Asandulesa M, Cozan V. Electrical conductivity of polyazomethine/fullerene C-60 nanocomposites. Phys Lett A 2017;381:796–800.

[30] Zhong M, Zeng W, Liu FS, Tang B, Liu QJ. Optical transparency, carrier mobility, and electrical conductivity of La-based copper layered oxychalcogenides: a density functional theory study. Sol Energy 2020;204:346–53.

[31] Liang GX, Zheng ZH, Fan P, Luo JT, Hu JG, Zhang XH, Ma HL, Fan B, Luo ZK, Zhang DP. Thermally induced structural evolution and performance of Sb_2Se_3 films and nanorods prepared by an easy sputtering method. Sol Energy Mater Sol Cells 2018;174:263–70.

[32] Wen X, Lu Z, Valdman L, Wang GC, Washington M, Lu TM. High-crystallinity epitaxial Sb_2Se_3 thin films on mica for flexible near-infrared photodetectors. ACS Appl Mater Interfaces 2020;12:35222–31.

[33] Ma Z, Chai S, Feng Q, Li L, Li X, Huang L, Liu D, Sun J, Jiang R, Zhai T, Xu H. Chemical vapor deposition growth of high crystallinity Sb_2Se_3 nanowire with strong anisotropy for near-infrared photodetectors. Small 2019;15:e1805307.

[34] Zhou Y, Leng MY, Xia Z, Zhong J, Song HB, Liu XS, Yang B, Zhang JP, Chen J, Zhou KH, Han JB, Cheng YB, Tang J. Solution-processed antimony selenide heterojunction solar cells. Adv. Energy Mater. 2014;4:1301846.

[35] Ren D, Chen S, Cathelinaud M, Liang GX, Ma H, Zhang X. Fundamental physical characterization of Sb_2Se_3-based quasi-homojunction thin film solar cells. ACS Appl Mater Interfaces 2020;12:30572–83.

[36] Luo YD, Tang R, Chen S, Hu JG, Liu YK, Li YF, Liu XS, Zheng ZH, Su ZH, Ma XF, Fan P, Zhang XH, Ma HL, Chen ZG, Liang GX. An effective combination reaction involved with sputtered and selenized Sb precursors for efficient Sb_2Se_3 thin film solar cells. Chem Eng J 2020;393:124599.

[37] Tao J, Hu X, Xue J, Wang Y, Weng G, Chen S, Zhu Z, Chu J. Investigation of electronic transport mechanisms in Sb_2Se_3 thin-film solar cells. Sol Energy Mater Sol Cells 2019;197:1–6.

[38] Ahn CW, Jo JH, Kim JC, Ullah H, Ryu S, Hwang Y, Choi JS, Lee J, Jeen H, Shin YH, Jeong HY, Kim IW, Kim TH. Highly ordered lead-free double perovskite halides by design. J. Materiomics 2020;6:651–60.

[39] Chen K, Wu P, Yang W, Su R, Luo D, Yang X, Tu Y, Zhu R, Gong Q. Low-dimensional perovskite interlayer for highly efficient lead-free formamidinium tin iodide perovskite solar cells. Nano Energy 2018;49:411–8.

Guangxing Liang is an associate researcher in College of Physics and Optoelectronic Engineering, Shenzhen University, Shenzhen, China. He obtained his PhD degree from University of Rennes 1, Rennes, France. He has extensive experience in solar energy materials and solar cells, including Sb_2Se_3, CZTS and perovskite, etc. He published over 100 science citation index (SCI) journal papers. He is regular journal paper reviewers for more than 10 journals. He is the academic editors of Advances in Materials Science and Engineering.

Shuo Chen is an assistant professor in College of Physics and Optoelectronic Engineering, Shenzhen University, China. He obtained his PhD degrees in Materials Science and Engineering from Zhejiang University, China, and Materials Science from University of Rennes 1, France. He focuses on the research of chalcogenide semiconductors, including the controllable synthesis of materials and applications as photoelectric devices.